PCCP

PAPER

View Article Online
View Journal | View Issue

Cite this: *Phys. Chem. Chem. Phys.*, 2025, **27**, 25624

Resolving spectral overlap in ENDOR by chirp echo Fourier transform detection

Julian Stropp,[a] Fabia Canonica,[b] Nino Wili *[c] and Daniel Klose *[a]

Electron nuclear double resonance (ENDOR) spectroscopy is a powerful technique for probing the structure and function of paramagnetic centers *via* measuring the magnetic interactions of unpaired electrons with nearby nuclear spins. For systems with multiple magnetic nuclei, commonly encountered in transition metal complexes in catalysis or metalloproteins, ENDOR spectra often become very crowded due to the broad, anisotropic hyperfine (HF) and nuclear quadrupole (NQ) interactions in disordered systems. In this work, we substitute the Hahn echo in Davies ENDOR by a chirp echo of the Kunz–Böhlen–Bodenhausen scheme to resolve spectral overlap in a second dimension. Fourier transformation of the chirp echo directly yields an additional EPR dimension without increasing measurement time and reveals correlations between nuclear and electron transitions, thereby resolving spectral overlap, shown here for ^{1}H, $^{14/15}$N and ^{63}Cu in ENDOR spectra of the copper protein ScoI. Different influences of interactions along the two dimensions and the possibility for selective excitation to address specific spectral components are exploited to disentangle the small copper NQ-coupling from the large, anisotropic HF-coupling. Simple, efficient frequency-domain simulations reproduce the experimental 2D Chirp Echo Epr SpectroscopY (CHEESY) ENDOR spectra and provide a basis to extract spin Hamiltonian parameters. Limitations and benefits of CHEESY ENDOR are discussed in comparison to established ENDOR techniques, 2D Mims ENDOR and HYEND, which reveals a competitive signal-to-noise ratio for CHEESY ENDOR due to the inherent FT advantage and RF-chirp compatibility to enhance sensitivity. These features expand the scope and feasibility of ENDOR investigations to a wider range of applications.

Received 2nd September 2025,
Accepted 13th November 2025

DOI: 10.1039/d5cp03372a

rsc.li/pccp

1 Introduction

Electron paramagnetic resonance (EPR) spectroscopy is uniquely suited to gain structural and functional insights into paramagnetic species. Due to the presence of unpaired electrons, these species are typically more reactive than their diamagnetic counterparts and are thus often encountered in chemically active sites. Over the years, EPR spectroscopy has provided detailed insights into the role of paramagnetic centers in homogeneous and heterogeneous catalysis,[1–6] metalloproteins,[7–9] and emerging functional materials such as quantum dots[10,11] and molecular magnets.[12] Continuous wave (CW) EPR is often the first step to detect and characterize the local environment of these centers. However, to access hyperfine interactions to ligand nuclei and their nuclear quadrupolar interactions, which are key to understanding the geometric and electronic structure around the paramagnetic center and are typically not resolved in CW EPR spectra, pulse EPR techniques such as electron nuclear double resonance (ENDOR) spectroscopy[13] or electron spin echo envelope modulation (ESEEM)[14,15] are required.

One of the most common ENDOR pulse sequences was introduced by Davies[16] and uses an initial selective microwave (MW) pulse to burn a "hole" into the inhomogeneously broadened EPR spectrum, followed by radiofrequency (RF) pulses that excite nuclear transitions connected with the initially inverted EPR transitions. The resulting change of the hole depth is detected *via* a Hahn echo sequence on the electron spins and reveals nuclear frequencies with line shapes that reflect the anisotropy of the hyperfine interaction. Mims ENDOR,[17] another established ENDOR experiment, employs a $\pi/2$–τ–$\pi/2$ preparation period to generate a polarization grid, making it more sensitive for the detection of weak hyperfine couplings. However, it introduces periodic blind spots in the spectrum, which affect the line shapes.[18] The structural information encoded in ENDOR spectra is normally extracted by fitting with parameters of an appropriate effective spin Hamiltonian and subsequent analysis of the resulting interaction

[a] *Department of Chemistry and Applied Bioscience, Institute for Molecular Physical Sciences, ETH Zürich, Vladimir-Prelog-Weg 2, 8093 Zürich, Switzerland. E-mail: daniel.klose@phys.chem.ethz.ch*
[b] *Department of Biology, Institute of Molecular Biology and Biophysics, ETH Zürich, Otto-Stern-Weg 5, 8093 Zürich, Switzerland*
[c] *Interdisciplinary Nanoscience Center, Aarhus University, Gustav Wieds Vej 14, 8000 Aarhus C, Denmark. E-mail: science@ninowili.ch*

parameters, often supported by model-based predictions from quantum chemical calculations.[19]

A major challenge in ENDOR spectroscopy is spectral overlap, especially in disordered systems such as powders and frozen solutions, where anisotropic interactions broaden peaks to several MHz. When multiple magnetic nuclei with similar resonance frequencies are involved, overlap can obscure individual interactions, complicating spectral assignment and simulation. This is particularly problematic in transition metal complexes, such as Ti-based olefin polymerization catalysts[20–24] or metalloproteins,[25,26] where signals from low-γ nuclei (^{13}C, $^{14/15}$N, ^{27}Al, ^{31}P, $^{35/37}$Cl, $^{47/49}$Ti, ...) often interfere with each other. Various strategies have been developed to address this issue: (1) a simple, but limited approach in Davies ENDOR spectroscopy is to adjust the selective inversion pulse length as a filter for the hyperfine coupling of interest, as was successfully applied to separate ^{14}N and ^{1}H peaks in X band.[27–30] (2) When hardware permits, an alternative approach is to change to a higher microwave frequency band, and thus higher magnetic field, spreading spectral features over a wider range.[31–33] High-field ENDOR features a high sensitivity and better orientation selection due to the larger effect of g-anisotropy on the EPR spectrum.[34] The smaller wavelength necessitates smaller sample volumes, which is advantageous if only small amounts are available, but can be infeasible especially for oxygen-sensitive, unstable samples.[20,35] (3) Finally, several two-dimensional (2D) ENDOR pulse sequences have been introduced to resolve overlap, albeit at the cost of longer acquisition times required due to sampling of the added dimension. Published approaches include 2D Mims ENDOR (Mims *versus* τ),[36,37] hyperfine correlated ENDOR (HYEND),[38,39] 2D TRIPLE[40,41] and chirp ENDOR-HYSCORE.[42]

In this work, we propose replacing the Hahn-echo detection block in the Davies ENDOR sequence by a chirp echo. This substitution enables broadband acquisition of the hole pattern in the EPR spectrum *via* Fourier transformation of the echo: EPR transitions linked through an NMR/ENDOR transition to the initially inverted transition (central hole) appear as side holes, with frequency offsets reflecting the hyperfine couplings. As a result, the EPR axis corresponds to an extra hyperfine dimension, resulting in a 2D ENDOR spectrum without extending the total measurement time compared to conventional Davies ENDOR. The concept of detecting the EPR hole pattern after the RF pulse in ENDOR dates back to the early days of pulse EPR spectroscopy, when fast arbitrary waveform generators for frequency-swept microwave (MW) pulses were not available. Early detection methods such as field-stepping during Hahn echo,[43] or rapid field scans under saturating MW and RF fields,[44,45] were limited by sensitivity and technical complexity. Later, Wacker and Schweiger used hard MW pulses to detect the free induction decay (FID) in ENDOR experiments.[46,47] Fourier transformation (FT) of the FID at each RF frequency directly correlated ENDOR and EPR transitions, improving measurement speed compared to previously reported experiments due to the FT-multiplex advantage. However, due to spectrometer deadtime, FID detection was only feasible for samples with narrow EPR spectra, such as single crystals. In addition, the bandwidth of a hard rectangular monochromatic pulse limits the highest hyperfine coupling that can be detected. With the advent of modern EPR instrumentation and fast arbitrary waveform generators, coherent frequency-swept (''chirp'') pulses have become feasible.[48] These enable chirp echoes following the Kunz–Böhlen–Bodenhausen approach[49,50] to overcome deadtime limitations and allow broadband EPR detection up to *ca.* 700 MHz.[48] Such chirp echoes have already been used in Chirp Echo EPR Spectroscopy (CHEESY)-detected NMR, a modified version of the electron-double-resonance-detected NMR (EDNMR) experiment.[24,51] Here, we demonstrate that chirp echo detection in the Davies ENDOR experiment reveals the hole pattern in the EPR spectrum. This approach reduces spectral overlap from different magnetic nuclei and eliminates the need for sampling an additional indirect dimension to obtain a 2D spectrum. Since quadrupolar couplings do not influence the electron spin transitions to first order, this method also simplifies the detection and assignment of quadrupolar interactions *via* their different influence along the two dimensions. In addition, the detection of resolved copper couplings shows that CHEESY ENDOR can be combined with chirped RF pulses[52] for sensitivity enhancement to detect strong, broadly distributed hyperfine interactions that may be lost or hard to discern in conventional 1D ENDOR spectra. With efficient open-source simulation scripts, based on EasySpin,[53] CHEESY ENDOR offers a powerful and versatile new method in hyperfine spectroscopy for detailed analysis of complex spin systems.

2 Experimental

2.1 Sample preparation

The α,γ-bisdiphenylene-β-phenylallyl (BDPA) sample was prepared by dissolving a 1 : 1 BDPA complex with benzene (CAS: 35585-94-5, Sigma-Aldrich Chemie GmbH, Steinfelden, Germany) in deuterated d_8-toluene (Sigma-Aldrich). 40 μL of the 500 μM solution were transferred into a 3.0 mm OD quartz tube (Aachener Quarzglas, Aachen, Germany) and flash frozen in liquid nitrogen. The isotope-labeled copper protein ScoI was prepared as described by Canonica *et al.*[54] The concentration of the (^{15}N, ^{63}Cu)-labeled ScoI·Cu^{2+} sample was 956 μM and of the ^{63}Cu-labeled ScoI·Cu^{2+} sample was 580 μM, each with 40 μL sample volume.

2.2 EPR spectrometer

All EPR spectra were acquired on a home-built arbitrary waveform generator (AWG)-based pulse X-/Q-band EPR spectrometer (to be published elsewhere) equipped with a cryogen-free variable temperature EPR cryostat (Cryogenic Ltd, London, UK) to maintain a stable sample temperature during the experiments. At X-band frequencies, a traveling wave tube (TWT) amplifier (Applied Systems Engineering, Inc., Forth Worth, USA) with a nominal output power of 1 kW was used together with an MD-4 ENDOR resonator (Bruker BioSpin, Ettlingen, Germany). The loaded *Q*-value of the resonator was 80 as determined by a

Lorentzian fit of the frequency response function (see section Pulse EPR experiments) and the maximum nutation frequency $\nu_{1,max}$ was 50 MHz. In Q band the setup included a TWT amplifier (Applied Sys. Eng., Inc.) with a nominal power of 100 W and a home-built oversized-sample Q-band ENDOR resonator[55] with a loaded $Q \approx 80$ and $\nu_{1,max}$ = 21 MHz. The RF pulses were generated with a separate AWG (HDAWG, Zurich Instruments, Zurich, Switzerland) and amplified with a 500 W RF amplifier (Amplifier Research Inc., Souderton, PA, USA).

2.3 Pulse EPR experiments

The setup and measurement procedure for all samples consisted of the following steps: (1) Recording an echo-detected field sweep spectrum. (2) Measuring the frequency response function of the excitation path including the resonator using frequency-swept nutation experiments at full MW power at the maximum of the EPR spectrum. (3) Measurement of T_1 and T_m with inversion recovery and Hahn echo experiments, respectively. (4) Setup of the chirp echo pulses according to the Kunz–Böhlen–Bodenhausen scheme: the bandwidth of the chirp pulses was chosen such that the strongest hyperfine couplings of interest lie well within the chirp bandwidth. The sweep-rate of the chirp pulses was adjusted to compensate for the frequency-dependent B_1-fields (see step (2)) and obtain an offset-independent adiabaticity during the pulse.[48,56] The optimal pulse amplitudes were determined with consecutive amplitude sweeps for the two pulses by maximizing the zero-frequency component in the Fourier transform of the echo. (5) Determining the AWG amplitude/power for the selective Gaussian-shaped inversion pulse using an amplitude sweep. (6) Recording Rabi oscillations using an RF pulse length sweep at a proton resonance frequency to obtain the B_2 strength. (7) Recording the CHEESY ENDOR spectrum with either a single frequency π RF pulse, or alternatively, a chirped RF pulse to increase the ENDOR sensitivity.

The X-band EPR data of BDPA were acquired at 9.78 GHz and 80 K with a shot repetition time of 100 ms. The echo-detected field sweep spectrum was recorded using a Hahn echo sequence with 16/32 ns pulses and an interpulse delay τ of 400 ns. The CHEESY ENDOR spectra were recorded at 348.8 mT with a 4-step phase cycle for the MW pulses (see SI). 200/100 ns long chirp pulses with 10 ns quarter sine shaped edges were used for a 200 MHz chirp echo. A delay τ of 1800 ns was used between the chirp pulses to allow for the detection of the full chirp echo. The ENDOR dimension was obtained by stepping the frequency of the 8 μs rectangular RF pulse linearly from 1 to 31 MHz. To reduce the effect of unwanted coherences from the inversion pulse and RF ringing a waiting time of 10 μs was used before and after the RF pulse. For comparison with the Davies ENDOR experiment the chirp echo detection was replaced by a 16–1600–32 ns Hahn echo.

The X-band ENDOR spectra of both ScoI samples were measured at 9.78 GHz and 20 K with a shot repetition time of 5 ms. The CHEESY ENDOR spectra were recorded at 340 mT, which is approximately in the center of the field-swept echo-detected EPR spectrum. The Gaussian inversion pulse had a length of 250 ns (FWHM). Pulses for the chirp echo and single frequency RF pulses had the same parameters as in BDPA experiments except for a shorter τ-value of 600 ns and a delay before the RF pulse of 1 μs. 2D Mims ENDOR was recorded using 10 ns π/2 pulses and 60 τ-values starting at 160 ns with increments of 8 ns. For HYEND a 250 ns Gauss pulse was used for selective inversion, two hard 10 ns MW pulses for the nuclear coherence transfer, and a 10–400–20 ns Hahn echo sequence for detection. The π/2 RF pulse length of 3 μs was chosen based on Rabi oscillations at different positions in the ENDOR spectrum. The nuclear echo was detected starting at 3.5 μs with 60 steps and a step size of 8 ns (see Fig. S5 for the influence of interpulse delays on the nuclear echo position). The total experimental time and the resolution of the hyperfine axis of both experiments was the same as for the CHEESY ENDOR experiment and hence the signal-to-noise ratio can be directly compared between the different spectra.

Q-band CHEESY ENDOR spectra were obtained at 15 K and 34.04 GHz with a shot repetition time of 20 ms. The spectrum was recorded at 1193.2 mT with a 100 ns Gaussian inversion pulse and 400 MHz chirp echo detection (300/150 ns pulses with 20 ns quarter-sine shaped edges, τ = 900 ns). The RF pulse was chirped with 500 kHz bandwidth and 40 μs pulse length to increase the sensitivity for broad copper peaks. The RF-frequency axis (2 to 98 MHz, 0.2 MHz resolution) was sampled stochastically to obtain the CHEESY ENDOR spectrum.

2.4 Data processing

CHEESY ENDOR echoes recorded at an intermediate frequency of around 1.4–1.8 GHz were offset-corrected and truncated to target length symmetrically around the echo center in post-processing (400 to 3000 ns for inversion pulse lengths of 100 ns to 500 ns, respectively). The echo was apodized with a Chebyshev window, zero-filled symmetrically on both sides and Fourier transformed. The frequency axis was shifted by subtracting the intermediate detection frequency. The FT spectrum of each echo was corrected for the hardware-dependent phase. If available, phases obtained from a chirp echo recorded without the Gaussian inversion pulse, were used for the correction. The CHEESY ENDOR spectrum was obtained by subtracting the real part of the FT spectrum with an off-resonance RF pulse (at the upper or lower end of the RF frequency sweep) from the real part of the FT spectrum at each ENDOR frequency. The 2D spectrum was normalized and plotted as a contour plot. The central hole of the 2D spectrum with EPR offsets smaller than the bandwidth of the Gaussian inversion pulse was integrated to obtain a conventional Davies ENDOR-like spectrum (for graphs above CHEESY ENDOR spectra). Signal-to-noise ratios in the comparison of 2D ENDOR experiments are calculated for three different peaks ($^1H_\alpha$: EPR: 2–12 MHz, ENDOR: 9–13 MHz; $^1H_\beta$: EPR: 12–25 MHz, ENDOR: 21–26 MHz; ^{15}N: EPR: 36–56 MHz, ENDOR: 18–28 MHz) by taking the mean of five values around the peak maximum as signal and the standard deviation of 100 points in a peak-free spectral region as noise level.

Experimental raw data including the experimental parameters for all measurements as well as data processing and visualization scripts in MATLAB (MathWorks Inc., Natick, MA) are available as open data.[57]

2.5 Simulations

Simulations of CHEESY ENDOR spectra were performed with home-written MATLAB scripts, which are based on earlier work by Wili *et al.*[58] and use the EasySpin library.[53] The simulation algorithm – originally used to simulate EDNMR spectra[59] – was adapted to include excitation of NMR transitions by RF pulses. In the algorithm, the evolution of spin populations is calculated for all combinations of EPR and ENDOR transitions, that lie within the pulse bandwidths. The inversion pulse is assumed to be Gaussian, and the population change during the RF pulse is modeled with the Bloch equation. The simulation does not include the chirp pulses, instead the ENDOR signal is calculated directly from the populations after the RF pulse, which introduces the largest deviation of the simulation to the experiment (see results/discussion). In the experiment the detection of the side holes is not only influenced by their transition probability, but additionally is scaled down by the transfer function of the detection arm mainly stemming from the resonator bandwidth. A detailed explanation of the algorithm is included in the SI, the simulation code is provided on zenodo with the URL **https://doi.org/10.5281/zenodo.17492056**.[57]

3 Results

3.1 BDPA: Working principle for a (S = 1/2, I = 1/2)-spin system

The working principle of CHEESY ENDOR is illustrated using the spectrum of the well-studied organic radical BDPA (Fig. 1),

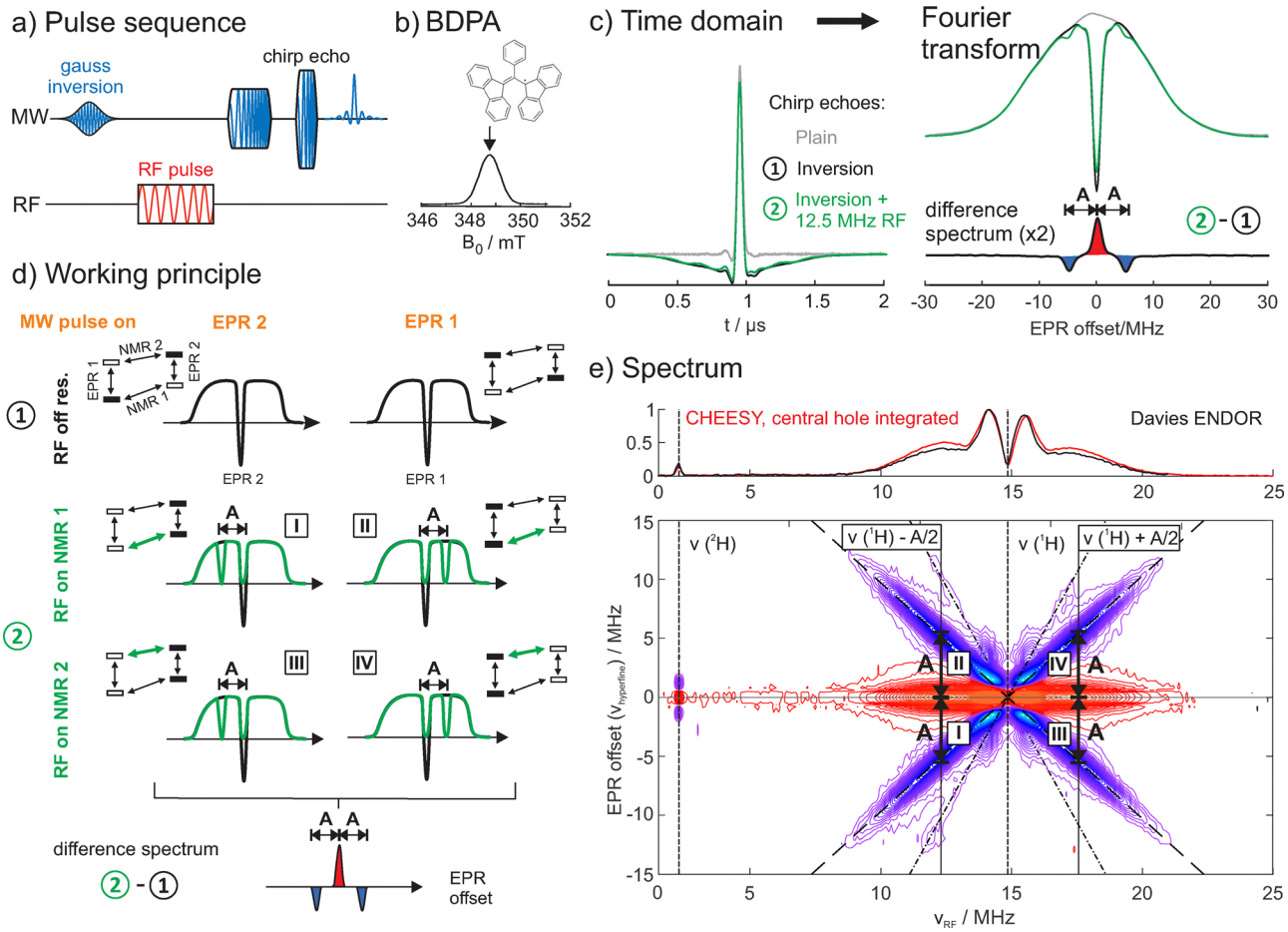

Fig. 1 Principle of 2D CHEESY ENDOR: correlating EPR and ENDOR transitions. (a) CHEESY ENDOR pulse sequence (b) Structure of BDPA radical and echo-detected field sweep X-band EPR spectrum with an arrow indicating the field used for CHEESY ENDOR. (c) Chirp echo of BDPA in time-domain and Fourier transformed chirp echo without (plain) and with MW and RF inversion pulses. (d) Population transfer and respective hole pattern in the EPR spectrum illustrates the working principle on an electron-nuclear 2-spin system with a hyperfine coupling that is unresolved in the EPR spectrum: depending on the RF pulse frequency six states with different population distributions can be detected in the EPR spectrum, *i.e.* along the EPR offset axis. Changes due to ENDOR transitions are best observed in the difference spectrum (RF on resonance – RF off resonance). (e) CHEESY ENDOR spectrum of BDPA with 500 ns selective Gaussian inversion pulse. Dashed vertical lines indicate the Larmor frequencies of ^{1}H and ^{2}H, diagonal lines indicate side hole ridges for the RF pulse inverting a single NMR transition (dashed) or two NMR transitions on different nuclei (dashed-dotted). Continuous vertical lines indicate the RF frequencies used in (d). The graph on top shows a normalized comparison of the integrated central hole (3 MHz width) of the CHEESY ENDOR spectrum to a Davies ENDOR experiment with Hahn echo detection.

which features a spin system with an unpaired electron ($S = 1/2$) coupled to multiple protons ($I = 1/2$).[60] By neglecting nuclear–nuclear interactions and considering only a single proton, the system simplifies to a two-spin model consisting of one electron and one nucleus. In the ENDOR experiment, the first MW pulse selectively inverts one of the two EPR transitions. This population inversion leads to a hole in the inhomogeneously broadened EPR spectrum of BDPA. The following, frequency-stepped RF pulse either excites one of the two NMR transitions or is off-resonant and does not change the populations in the spin system (Fig. 1(d)). In the case when the pulse is on resonance with one of the NMR transitions, a part of the original center hole intensity is transferred to a side hole located at the frequency of the connected EPR transition. The frequency difference between center and side holes corresponds to the hyperfine coupling. For a perfect RF π pulse both EPR transitions become depolarized; the center hole and side hole both reach down to zero intensity. The chirp echo at the end of the pulse sequence enables broadband EPR detection, which covers the whole EPR spectrum of BDPA, including the side hole pattern. The CHEESY ENDOR spectrum is obtained by Fourier transformation of the echo for each RF frequency and subsequent subtraction of the Fourier-transformed echo at an off-resonant RF frequency (Fig. 1(c)). In conventional Davies ENDOR integration of the Hahn echo detects only the central hole intensity as function of the RF frequency, and accordingly the Davies ENDOR spectrum is found along the horizontal axis in CHEESY ENDOR (Fig. 1(e)). Since hard MW pulses completely excite the narrow EPR spectrum of BDPA, Fourier transformation of a Hahn echo would convey the same information as a chirp echo with side holes having a smaller intensity due to the reduced bandwidth. For spin systems with larger couplings a chirp echo with higher bandwidths is required to detect the complete hole and side hole pattern in the EPR spectrum. Side holes appear on either side of the central hole because the EPR spectrum is inhomogeneously broadened, allowing the selective microwave inversion pulse to excite both of the two EPR transitions (Fig. 1(d)). The side holes are shifted by the hyperfine coupling constant A from the central hole and have the opposite sign in the difference spectrum compared to the central hole. Since BDPA has many protons with anisotropic hyperfine couplings up to 10 MHz (Table S1),[60] no individual side holes for each proton are observed, but an "x"-shaped continuous side hole pattern forms ridges (dashed lines along ($\nu_L(^1H) \pm A/2, \pm A$) in Fig. 1(e)). Very weak side hole ridges with a shift of $2A$ from the central hole (dash-dotted lines in Fig. 1(e)) appear in the spectrum because two NMR transitions of the same frequency, originating from different protons coupled to the same electron spin, can be simultaneously excited with a small probability. Additionally, at low RF frequencies a deuterium peak is observed due to the small coupling of the electron spin to deuterium spins of the solvent d_8-toluene. The almost perfect overlap of the normalized spectra in Fig. 1(e) (top) illustrates that the integrated central hole in CHEESY ENDOR contains the same information as the conventional Hahn echo-detected Davies ENDOR spectrum.

Information on the resolution in ENDOR experiments can be inferred from the linewidth of the holes in the CHEESY ENDOR spectrum. The bandwidth of the selective MW inversion pulse determines the EPR hole width and thereby the resolution along the EPR offset axis, which is also called hyperfine axis as introduced by Bühlmann *et al.*[43] Further, as visible in Fig. S1, the initial inversion pulse also influences the sensitivity of the experiment for different hyperfine couplings.[18,29] Shorter π-inversion pulses are less sensitive to detect smaller hyperfine couplings, since the pulse becomes less selective and hence the central hole becomes broader. Simulations of BDPA spectra for three different MW pulse lengths reproduce the experimental hyperfine selectivity (Fig. S1, see Table S1 for spin Hamiltonian parameters from literature[60]). The resolution along the ENDOR axis is determined by the bandwidth of the RF pulse (power broadening)[32] or the NMR linewidth, which is limited by unresolved nuclear–nuclear dipolar interactions.[61,62] The shortest experimentally achievable RF π pulses are on the order of several μs long. For broad, anisotropic hyperfine couplings, as typically found in disordered systems of transition metal complexes, the achievable bandwidth of rectangular RF pulses (about 10–100 kHz) is often smaller than the sharpest features of the ENDOR spectrum and hence the shortest pulses with highest RF power are used to obtain the highest ENDOR sensitivity. For the spectrum of BDPA the strong RF pulse (8 μs) determines the ENDOR resolution (line width), yet this is still small compared the broad and distributed ^{1}H couplings. Since the ENDOR resolution (10–100 kHz) exceeds the EPR resolution (1–10 MHz), the width of the Gaussian inversion pulse dominates the peak shape in 2D CHEESY ENDOR spectra (*cf.* Fig. S1).

3.2 ScoI-Cu: Resolving spectral overlap in a multi-nuclear spin system with $I > 1/2$-nuclei

The advantage of CHEESY ENDOR over conventional Davies ENDOR is revealed for samples with significant spectral overlap, *i.e.* with more complicated spin systems as for ScoI-Cu^{2+}. ScoI is a copper metallochaperone found in both bacteria as well as Eukaryotes, where it is involved in the complex biogenesis of the Cu_A-center of CoxB, a subunit of the terminal enzyme cytochrome oxidase (Cox) of the respiratory chain found in the mitochondrial or the plasma membranes in eukaryotes or prokaryotes, respectively.[54] While the crystal structure of bacterial ScoI-Cu^{2+} is known (PDB: 4WBR, see Fig. 2(a)), the structures of complexes during the formation of Cu_A-CoxB mediated by ScoI-Cu^{2+} remain elusive up to now. This turns ScoI into an interesting and relevant model system to establish and evaluate pulse EPR techniques, which can later be used to investigate unknown Cu–protein complexes. ScoI features a single Cu(II) center in a distorted square planar environment with two cysteine and one histidine ligands from the protein and a free, coordinating water molecule as a fourth ligand. The spin Hamiltonian parameters of the system were determined previously using CW EPR,[54] EDNMR, HYSCORE and ENDOR at X- and Q-band frequencies[63] and are used for CHEESY ENDOR simulations (see Table S2).

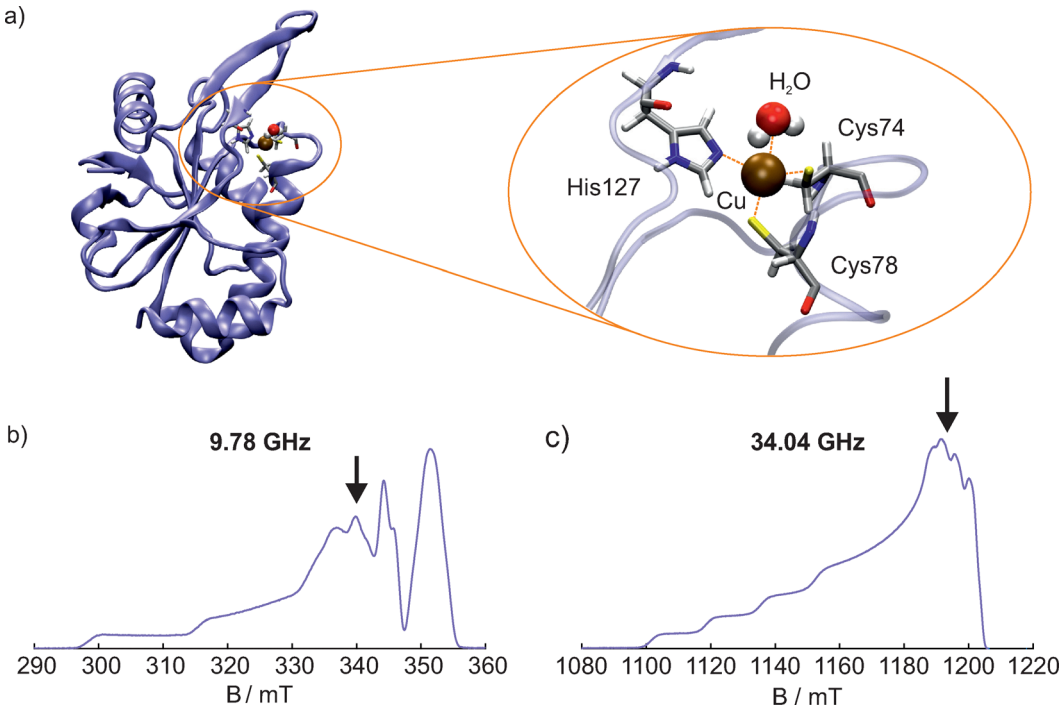

Fig. 2 (a) Protein structure of ScoI·Cu^{2+} (PDB ID: 4WBR[54]) with a zoom into the distorted square planar coordination of the copper binding site. Echo-detected field sweep EPR spectra of (^{15}N, ^{63}Cu)-labeled ScoI·Cu^{2+} in (b) X band and (c) Q band. Field positions used for ENDOR experiments are marked with an arrow.

The X-band CHEESY ENDOR spectrum of (^{15}N, ^{63}Cu)-labeled ScoI measured at the center of the EPR spectrum (Fig. 2(b)) shows ^{15}N-peaks that are well-separated from proton peaks (Fig. 3(a), left) in the EPR/hyperfine dimension. Slices through the 2D spectrum at certain RF frequencies reveal that central and side hole intensities are less than 10% of the Fourier-transformed chirp echo intensity (Fig. S3). The 1D spectrum, obtained by integrating the central hole (Fig. 3(a), top), illustrates that the nitrogen peaks spanning from 18 to 28 MHz would be concealed by the more intense proton peak at this frequency in 1D Hahn echo-detected Davies ENDOR spectra. The use of a selective, 250 ns-long Gaussian inversion pulse provides sufficient resolution to resolve the two narrowly separated nitrogen peaks from different electron spin manifolds. This shows that CHEESY ENDOR not only resolves overlap of peaks from different nuclei, but also simplifies the read-out and simulations of peak pairs of the same nucleus. Simulations with two protons and a strongly coupled nitrogen show an almost perfect agreement with the experimental spectrum (Fig. 3(a), right). Besides the substantial overlap, the primary qualitative difference between experiment and simulation is the presence of two horizontal side hole ridges at an EPR offset of $\pm\nu_L(^1H) = \pm 14.3$ MHz. These ridges arise from so-called forbidden transitions involving both the electron and matrix protons excited during the selective microwave inversion pulse, similar to matrix peaks in EDNMR.[51] After the selective MW inversion pulse, if the subsequent RF pulse excites an NMR transition, the holes – whether created *via* allowed transitions (central hole at 0 MHz) or forbidden transitions (side holes at ± 14.3 MHz) – all become shifted by the hyperfine coupling. The observed intensity pattern arises because in the difference spectrum, positive intensities correspond to holes generated by the MW inversion pulse, while negative intensities arise from holes created by the RF pulse. Hence the holes resulting from forbidden transitions are easily identified by their positive intensity at $\nu_{hyperfine} \neq 0$ MHz and also clearly understood. The polarization transfer pathway leading to these peaks, a forbidden transition followed by a nuclear transition, is the same as in the triple resonance hyperfine sublevel correlation spectroscopy (THYCOS) sequence, which utilizes a long high turning angle pulse instead of the short Gaussian inversion pulse to correlate NMR transitions of the same electron spin manifold and the same paramagnetic center.[64] Although these forbidden transitions are rather unwanted for the 2D CHEESY ENDOR spectrum of ScoI, they imply that chirp echo detection may be used in 2D THYCOS experiments as well to reduce the number of indirectly sampled dimensions. The probability of exciting forbidden transitions depends on the length of the inversion pulse as well as the magnetic field and the corresponding peaks disappear in higher frequency bands (see Q-band spectrum in Fig. 3(c)). The CHEESY ENDOR simulations would reproduce these peaks, if matrix protons were included in the spin system. They are omitted in the simulation, since the computing time scales exponentially with the number of nuclei and no additional information is gained. The relative central hole intensities of the simulations differ from the experiment in Fig. 3(a) (top) since simulated spectra are not broadened beyond the pulse profiles (relaxation, unresolved hyperfine splittings, and

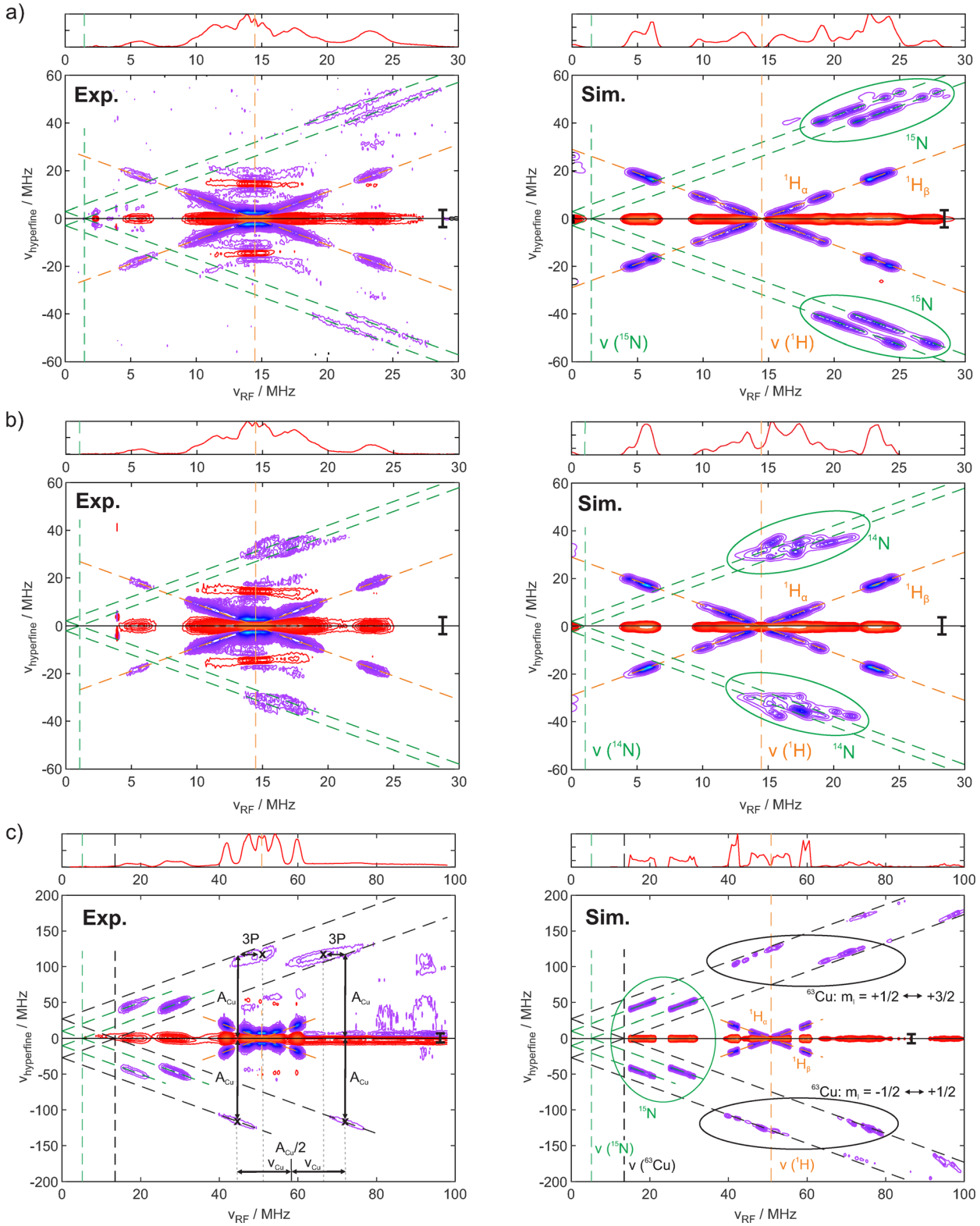

Fig. 3 Deconvolution of ^{1}H, $^{14/15}$ N and previously ambiguous $A_\perp$(^{63}Cu) couplings in ScoI with CHEESY ENDOR. Experimental CHEESY ENDOR spectra (left) and simulations (right) with positive peaks in red and negative peaks in blue: (a) (^{15}N, ^{63}Cu)-labeled ScoI·Cu^{2+} at 340 mT and 9.78 GHz; (b) ^{63}Cu-labeled ScoI·Cu^{2+} at 340 mT and 9.78 GHz; (c) (^{15} N, ^{63}Cu)-labeled ScoI·Cu^{2+} at 1194 mT and 34.04 GHz. Larmor frequencies of detected nuclei and their calculated side hole ridges based on their hyperfine coupling are indicated by dashed lines. Points indicated with "*x*" in (c) correspond to one set of effective copper couplings (*A*, 3*P*) and are accompanied with annotations to showcase the estimation of couplings from the experimental spectrum (see Fig. S4 for a schematic energy level diagram and the corresponding ENDOR stick spectrum). The 1D spectra on top show the integrated central hole intensity around $\nu_{hyperfine}$ = 0 MHz (integration window is marked by a black scale bar in all CHEESY ENDOR spectra). Simulation parameters can be found in Table S2.

distributions in magnetic parameters are not included) and the two protons of the simulation do not represent the larger total number of protons present in ScoI.

In the spectrum of ScoI with natural abundance nitrogen (Fig. 3(b)) the ^{14}N peaks appear at smaller ENDOR and EPR frequencies compared to ^{15}N since the Larmor frequency and hyperfine coupling are scaled down by $\nu_L(^{14}N)/\nu_L(^{15}N) = -0.71$. The nuclear quadrupolar coupling leads to an additional splitting of the ^{14}N-peaks along the ENDOR dimension. Since the quadrupolar coupling is small compared to the hyperfine coupling and a large number of different orientations is excited at this magnetic field position, the four different NMR transitions overlap in the CHEESY ENDOR spectrum. A longer selective pulse can be used to separate the peaks at the expense of sensitivity and thus significantly longer acquisition time. Nevertheless, the simulation correctly reproduces the peak pattern of the experiment, showcasing its suitability for spin systems with multiple spins and $I > 1/2$. The effect of the quadrupolar coupling in CHEESY ENDOR spectra is best explained with the resolved copper peaks in Q-band spectra of (^{15}N, ^{63}Cu)-labeled ScoI (Fig. 3(c)). In contrast to X-band ENDOR, in Q band the nitrogen peaks are well separated from the proton peaks, but weak copper peaks at $A/2$ = 40–80 MHz overlap with the proton peaks in one-dimensional ENDOR spectra recorded at the high field end of the EPR spectrum. Since anisotropic copper HF-couplings are commonly significantly larger than copper NQ-couplings, EPR spectroscopists often only determine axial HF-couplings based on CW EPR experiments and attempts to resolve the full HF- and NQ-coupling tensor with ENDOR spectroscopy are rarely performed.[65,66] Side holes due to the copper NMR transitions become visible in the CHEESY ENDOR spectrum (Fig. 3(c)) when using a 500 kHz chirped RF pulse to increase sensitivity.[52] Since here the copper hyperfine coupling $A_\perp$ is partially resolved in the EPR spectrum, the selective MW pulse predominantly excites the EPR transition with $m_I(^{63}Cu) = +1/2$ (see Fig. S4a for a qualitative energy level diagram). The copper side holes at positive and negative EPR offsets in the CHEESY ENDOR spectrum correspond to different EPR transitions. The side hole at the negative EPR offset ($m_I(^{63}Cu) = -1/2$) is connected to the center hole by the central NMR transitions, that are, to first order, unaffected by quadrupole coupling. They have transition frequencies of $\nu_{m_I=+1/2\leftrightarrow+3/2} = A_\perp/2 \pm \nu_L \mp 3P$ depending on the electron spin manifold and thus the side hole peaks align precisely with the black line representing the calculated hole positions for nuclei without quadrupole interaction. The peaks with a positive EPR offset ($m_I(^{63}Cu) = +3/2$) are linked to the ENDOR transitions with $\nu_{m_I=+1/2\leftrightarrow+3/2} = A_\perp/2 \pm \nu_L \mp 3P$ and are shifted horizontally from the black line. Since, to first order, only the ENDOR dimension is affected by the shift, the nuclear quadrupole coupling constant $3P$ of Cu(II) can be determined from the horizontal offset (illustrated by horizontal lines in Fig. 3(c)). The simulation correctly reproduces the entire two-dimensional spectrum including the direction of the shift due to the nuclear quadrupole coupling. Yet, clearly, the simulated shift is smaller than in the experimental spectrum possibly due to an underestimated nuclear quadrupole coupling or an imprecision of the exact orientation selection and magnetic field position. Peaks at large EPR offsets appear more prominently in the simulation than in the experiment, since the detection efficiency for large offsets from the center frequency in the experiment is suppressed by the transfer function of the detection arm mainly stemming from the limited bandwidth characteristics of the resonator.[48]

4 Discussion

The spectra of Cu(II)-ScoI highlight the applicability of CHEESY ENDOR to resolve spectral overlap. The experiment is assessed compared to other 2D ENDOR techniques namely 2D Mims ENDOR and HYEND spectra for ScoI recorded with the same total measurement time and similar resolution as in the CHEESY ENDOR experiment (Fig. 4, Fig. S6 and Table 1). The 2D Mims ENDOR spectrum is obtained by incrementing the τ value and subsequent Fourier transformation along the τ dimension.[36] Here, the strongly coupled nitrogen peaks are barely visible, showing that 2D Mims ENDOR is more sensitive for small hyperfine couplings. The hyperfine resolution is limited by the phase memory time T_m, which may interfere with the effectiveness of Mims ENDOR for detecting sharp features in small couplings.[18] The spectrum shows the highest background of all three 2D experiments with a peak at $\nu_{hyperfine}$ = 14.3 MHz, ν_{ENDOR} = 14.3 MHz that possibly arises due to forbidden transitions with matrix protons. HYEND is based on the Davies ENDOR experiment with a nuclear evolution time between two RF π/2 pulses instead of the single RF π pulse.[38] The HYEND spectrum in Fig. 4(b) shows a clear peak separation with no peaks due to forbidden transitions as discernible in CHEESY ENDOR. Here, the hyperfine resolution is determined by the decay rate of the nuclear oscillations during the central evolution time t_{nuc}. This decay rate is typically set by the length of the RF π/2 pulses as they define the bandwidth of excited ENDOR frequencies and thereby the dispersion of nuclear frequencies (see Fig. S5).[38] If the RF pulses are long, the echo decay may become limited by the transverse nuclear spin relaxation time T_{2n}. Assuming that the coupling to the fluctuating electron spin is the dominant contribution to nuclear relaxation, T_{2n} is constrained by the electron spin relaxation time T_{1e}.[67] A disadvantage of HYEND compared to other techniques is that using chirped RF pulses to enhance sensitivity may be more challenging for π/2 pulses than for π pulses.

CHEESY ENDOR requires a spectrometer setup with an AWG to create the MW chirp pulses that allows for transient echo detection. It differs from the other two techniques in that both positive and negative peaks are detected, which readily separates the desired side hole pattern from contributions due to the central hole (ENDOR) and those induced by forbidden transitions. For this purpose, CHEESY ENDOR requires a minimum chirp echo bandwidth of two times the size of the largest hyperfine coupling to be detected. Hence, the typical

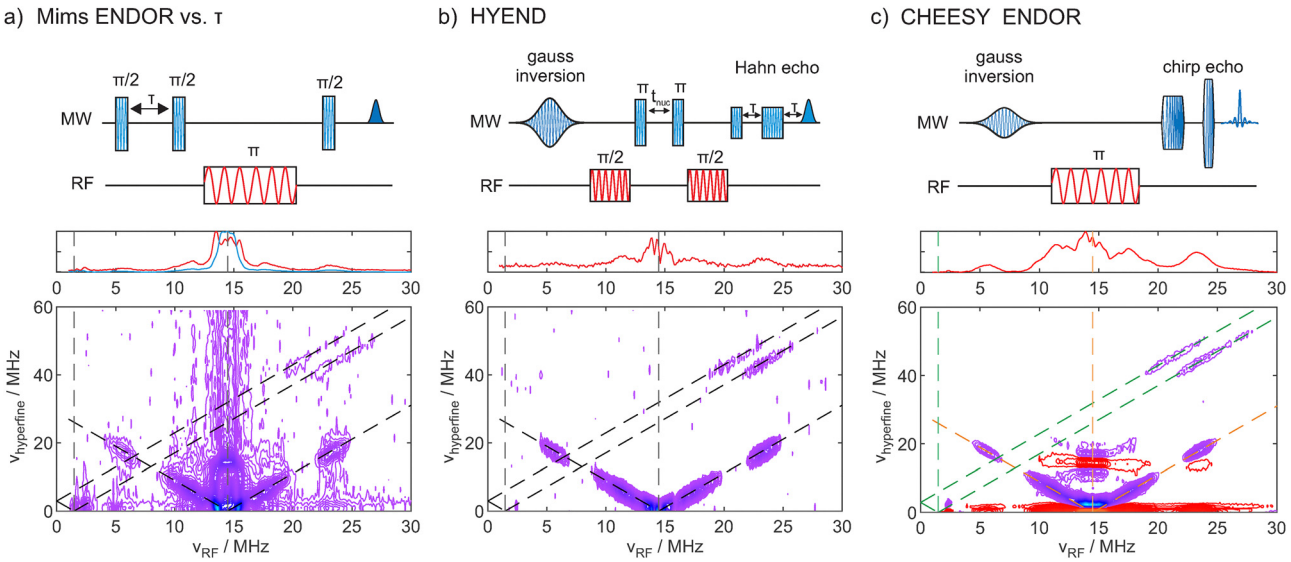

Fig. 4 Comparison of CHEESY ENDOR to established 2D ENDOR experiments with a hyperfine dimension for (^{15}N, ^{63}Cu)-labeled ScoI·Cu^{2+} in X band, at 340 mT, with the same measurement time: (a) 2D Mims ENDOR with 60 τ-values starting at 160 ns and increments of 8 ns. The 1D trace shows the sum of the Mims ENDOR spectra (blue) and the sum of the 2D FT spectrum (red). (b) HYEND with a 250 ns Gaussian inversion pulse and t_{nuc} with 60 steps of 8 ns. The 1D trace shows the sum of the 2D FT spectrum. (c) 2D CHEESY ENDOR spectrum with 250 ns Gaussian inversion pulse and the integrated central hole intensity (top). The bottom half ($\nu_{hyperfine} < 0$ MHz) was added onto the top half of the 2D spectrum. Larmor frequencies and side hole ridges for ^{1}H and ^{15}N are marked with dashed lines.

MW power required to support such chirp echoes, even up to about 100–200 MHz is less than for ultra-wide band chirp echo experiments.[56] The multiplex advantage of the chirp echo detection comes with two limitations compared to methods based on echo integration: (1) the sensitivity in the hyperfine dimension depends on the resonator transfer function with signals at larger offsets from the resonator dip being detected less efficiently (*cf.* Fig. S3).[48] As a result, the nitrogen peaks at $\nu_{hyperfine} \approx 50$ MHz have only a slightly higher S/N ratio than in HYEND and 2D Mims ENDOR (see Table 1). The sensitivity for large couplings can be increased by using a more broadband resonator (or by shifting frequency of the resonator dip from the center hole to the side hole of interest). (2) The sensitivity in detecting the center frequency of the chirp echo is reduced compared to a Hahn echo, which has been observed previously.[48] In the spectra of ScoI the intensity at $\nu_{hyperfine} = 0$ MHz is reduced to *ca.* 80% in X band and to *ca.* 50% in Q band (see Fig. S2). This sensitivity decrease originates from chirp pulses suffering from hardware-related distortions, and also due to a faster decay ($1/T_m$) of chirp echoes.[48] The instantaneous diffusion contribution to $1/T_m$ scales with the number of excited spins[48,68,69] and makes broadband chirp echoes for samples with high spin concentrations less sensitive than expected (Fig. S2). The echo decay rate $1/T_m$ decreased from $T_m \approx 2.1$ µs for a 16/32 ns Hahn echo sequence down to 1.8 µs (200 MHz) and 1.5 µs (300 MHz) for chirp pulses in X band for ScoI·Cu^{2+} (Fig. S2c). Since sufficiently long τ-values are required to observe the longer echoes due to the selective Gaussian inversion pulse in ENDOR, the faster echo decay reduces the sensitivity advantage of CHEESY ENDOR compared to conventional Davies ENDOR. To mitigate this effect, the bandwidth of the chirp pulses should be as small as feasible and the shortest possible τ-value should be chosen, thus these relations present an experimental tradeoff. Alternatively, if the chirp echo decay is especially fast, it may be advantageous to decrease the τ-value to increase echo intensity, with the echo time approximately matching the deadtime, and to Fourier transform only the second half of the chirp echo, while the first half is lost in the spectrometer deadtime.

The comparison for (^{15}N, ^{63}Cu)-labeled ScoI·Cu^{2+} in Fig. 4 and Table 1 shows that CHEESY ENDOR can compete with other 2D techniques and is often favorable due to the inherent multiplex advantage. The advantage of CHEESY ENDOR becomes more pronounced for nuclei with $I > 1/2$, as observed

Table 1 Comparison of selected 2D ENDOR techniques shown in Fig. 4

Experiment	2D Mims ENDOR	HYEND	CHEESY ENDOR
Hardware requirements	Standard ENDOR spectrometer	Coherent RF pulse generation	MW AWG for chirp echo detection
Target hyperfine coupling size	Small	Large	Large
NQI-influence along $\nu_{hyperfine}$	Not to 1. order	Yes	Not to 1. order
Resolution along $\nu_{hyperfine}$	Limited by T_m	Limited by $t_{p(\pi/2,RF)}$ or T_{2n}	Limited by inversion pulse bandwidth
Implementation of chirp RF pulses	Easy	Difficult/decrease $\nu_{hyperfine}$-resolution	Easy
Experimental signal/noise ratio	$^{1}H_{\alpha}$: 97, $^{1}H_{\beta}$: 38, ^{15}N: 7	$^{1}H_{\alpha}$: 63, $^{1}H_{\beta}$: 38, ^{15}N: 8	$^{1}H_{\alpha}$: 150, $^{1}H_{\beta}$: 51, ^{15}N: 13

for ^{14}N-labeled ScoI·Cu^{2+}, for which ^{14}N ridges are exclusively detected by CHEESY ENDOR (Fig. S6). Multiple options are available to tailor the CHEESY ENDOR experiment to the specific task at hand: (1) The inversion pulse length can be adapted to the coupling size and targeted resolution. More advanced inversion pulse shapes as described by Tait and Stoll may provide a benefit compared to the Gaussian pulses used in this work.[70] (2) Chirped RF pulses can be used to enhance t he sensitivity.[52] (3) Even though the chirp echo performance depends on the resonator specifications, it can be optimized without changing the hardware by shifting the center frequency from the dip center or by exchanging the Kunz–Böhlen–Bodenhausen chirp echoes with different excitation schemes, such as the CHORUS (CHirped ORdered pulses for ultra-broadband spectroscopy) pulse sequence for a more uniform excitation bandwidth.[71] Overall, chirp echo detection in Davies ENDOR not only correlates NMR and EPR transitions in two dimensions, but also reveals processes such as forbidden transitions excited by the Gauss inversion pulse that are not visible in conventional 1D ENDOR spectra. The implementation of chirp echo detection is not limited to Davies ENDOR, but may also be beneficial for other ENDOR techniques (2D TRIPLE,[41] THYCOS[64]) and can be applied in combination with high-field experiments in the future. In the broader context, these developments demonstrate the potential of chirp echoes in ENDOR to assist in the characterization of complex paramagnetic centers *via* the additional hyperfine dimension. We envisage that CHEESY ENDOR may substitute conventional 1D Davies ENDOR in the elucidation of spin centers with several magnetic nuclei, since the slight loss in sensitivity is outweighed by the gain in resolution. The tunability of the pulses to the task at hand and the separability of nuclear quadrupolar and hyperfine interactions along the two dimensions together with the efficient simulation algorithm turn CHEESY ENDOR into an excellent tool to obtain highly-resolved information on the structure and function of paramagnetic systems suitable for a considerable variety of applications.

5 Conclusions

Chirp echo detection in Davies ENDOR experiments with subsequent Fourier transformation of the echoes results in a 2D spectrum that correlates nuclear frequencies with EPR transitions, without the need to sample an additional indirect dimension. On the example of the metalloprotein ScoI·Cu^{2+}, we show that CHEESY ENDOR significantly reduces spectral overlap by resolving ENDOR peaks along a second dimension. In X band the common overlap of ^{1}H and strongly coupled ^{14}N-peaks was resolved, and in Q band we were able to distinguish broad, anisotropic copper peaks from ^{1}H peaks and estimate the copper nuclear quadrupole interaction as an offset along the ENDOR frequency axis. Simulations based on home-written, open-source scripts correctly reproduce the experimental features and provide a basis for efficient spectral analysis of unknown systems. A comparison with the two other techniques, 2D Mims ENDOR and HYEND, shows competitive or superior sensitivity and resolution for CHEESY ENDOR. Yet when comparing to the number of initially excited spins, the multiplex advantage of CHEESY ENDOR remains somewhat below expectations due to the lower detection sensitivity with the current chirp echoes – an aspect warranting further improvement. The increased sensitivity and adaptability of CHEESY ENDOR renders it a valuable and versatile new approach within the realm of hyperfine spectroscopy interesting for both exploratory as well as accuracy-focused investigations.

Author contributions

JS: conceptualization, formal analysis, investigation, methodology, software, validation, visualization, writing – original draft; FC: sample preparation and quality control, writing – review and editing; NW: conceptualization, formal analysis, investigation, methodology, software, supervision, validation, visualization, writing – review and editing; DK: conceptualization, sample preparation and quality control, formal analysis, investigation, methodology, funding acquisition, project administration, resources, supervision, validation, visualization, writing – review and editing.

Conflicts of interest

There are no conflicts to declare.

Data availability

Additional results supporting this article have been included as part of the supplementary information (SI). Supplementary information is available. See DOI: **https://doi.org/10.1039/d5cp03372a**.

Raw data as well as processing, plotting and simulation scripts in MATLAB are deposited on zenodo with the URL **https://doi.org/10.5281/zenodo.17492056**.[57]

Acknowledgements

Financial support from ETH research grant (ETH-35221) to DK is gratefully acknowledged. The authors would like to acknowledge Prof. Gunnar Jeschke for helpful disucssions on HYEND experiments. Prof. Rudi Glockshuber is gratefully acknowledged for sharing the ScoI plasmids as well as wetlab access for sample preparation.

References

1 S. Van Doorslaer and D. M. Murphy, *EPR Spectroscopy in Catalysis*, Springer, Berlin Heidelberg, 2011, p. 139.
2 E. Morra, S. Maurelli, M. Chiesa and E. Giamello, *Top. Catal.*, 2015, **58**, 783–795.
3 D. Goldfarb, *Phys. Chem. Chem. Phys.*, 2006, **8**, 2325.

4 M. M. Roessler and E. Salvadori, *Chem. Soc. Rev.*, 2018, **47**, 2534–2553.
5 S. A. Bonke, T. Risse, A. Schnegg and A. Brückner, *Nat. Rev. Methods Primers*, 2021, **1**, 1–20.
6 F. Hecker, J. Stubbe and M. Bennati, *J. Am. Chem. Soc.*, 2021, **143**, 7237–7241.
7 S. Van Doorslaer and E. Vinck, *Phys. Chem. Chem. Phys.*, 2007, **9**, 4620.
8 *High Resolution EPR: Applications to Metalloenzymes and Metals in Medicine*, ed. L. Berliner and G. Hanson, Springer, New York, 2009.
9 J. Eisermann, M. Seif-Eddine and M. M. Roessler, *Curr. Opin. Chem. Biol.*, 2021, **61**, 114–122.
10 P. G. Baranov, S. B. Orlinskii, C. de Mello Donegá and J. Schmidt, *Appl. Magn. Reson.*, 2010, **39**, 151–183.
11 J. K. Bindra, K. Singh, J. van Tol, N. S. Dalal and G. F. Strouse, *J. Phys. Chem. C*, 2020, **124**, 19348–19354.
12 J. van Slageren, *New Directions in Electron Paramagnetic Resonance Spectroscopy on Molecular Nanomagnets*, Springer, Berlin Heidelberg, 2011, pp. 199–234.
13 G. Feher, *Phys. Rev.*, 1956, **103**, 834–835.
14 L. G. Rowan, E. L. Hahn and W. B. Mims, *Phys. Rev.*, 1965, **137**, A61–A71.
15 W. B. Mims, *Phys. Rev. B: Condens. Matter Mater. Phys.*, 1972, **5**, 2409–2419.
16 E. Davies, *Phys. Lett. A*, 1974, **47**, 1–2.
17 W. B. Mims, *Proc. R. Soc. London, Ser. A*, 1965, **283**, 452–457.
18 J. R. Harmer, *Hyperfine Spectroscopy – ENDOR*, John Wiley & Sons, Ltd, 2016, pp. 1493–1514.
19 F. Neese, *Quantum Chemistry and EPR Parameters*, John Wiley & Sons, Ltd, 2017, pp. 1–22.
20 M. Inoue, J. Stropp, A. Ashuiev, Y. Kakiuchi, P.-A. Payard, T. Teraishi, M. Mizukami, H. Tsurugi, D. Klose, C. Copéret and K. Mashima, *J. Am. Chem. Soc.*, 2025, **147**, 16438–16449.
21 E. Salvadori, M. Chiesa, A. Buonerba and A. Grassi, *Chem. Sci.*, 2020, **11**, 12436–12445.
22 E. Morra, E. Giamello and M. Chiesa, *J. Magn. Reson.*, 2017, **280**, 89–102.
23 S. Van Doorslaer, J. J. Shane, S. Stoll, A. Schweiger, M. Kranenburg and R. J. Meier, *J. Organomet. Chem.*, 2001, **634**, 185–192.
24 A. Ashuiev, F. Allouche, N. Wili, K. Searles, D. Klose, C. Copéret and G. Jeschke, *Chem. Sci.*, 2021, **12**, 780–792.
25 P. Dorlet, S. Gambarelli, P. Faller and C. Hureau, *Angew. Chem., Int. Ed.*, 2009, **48**, 9273–9276.
26 S. Van Doorslaer, G. M. Cereghetti, R. Glockshuber and A. Schweiger, *J. Phys. Chem. B*, 2001, **105**, 1631–1639.
27 C. Bolm, M. Martin, G. Gescheidt, C. Palivan, D. Neshchadin, H. Bertagnolli, M. Feth, A. Schweiger, G. Mitrikas and J. Harmer, *J. Am. Chem. Soc.*, 2003, **125**, 6222–6227.
28 C. Bolm, M. Martin, G. Gescheidt, C. Palivan, T. Stanoeva, H. Bertagnolli, M. Feth, A. Schweiger, G. Mitrikas and J. Harmer, *Chem. – Eur. J.*, 2007, **13**, 1842–1850.
29 C. Fan, P. E. Doan, C. E. Davoust and B. M. Hoffman, *J. Magn. Reson.*, 1992, **98**, 62–72.
30 P. E. Doan, C. Fan, C. E. Davoust and B. M. Hoffman, *J. Magn. Reson.*, 1991, **95**, 196–200.
31 I. García-Rubio, M. Fittipaldi, F. Trandafir and S. Van Doorslaer, *Inorg. Chem.*, 2008, **47**, 11294–11304.
32 J. Harmer, C. Finazzo, R. Piskorski, C. Bauer, B. Jaun, E. C. Duin, M. Goenrich, R. K. Thauer, S. Van Doorslaer and A. Schweiger, *J. Am. Chem. Soc.*, 2005, **127**, 17744–17755.
33 M. M. Werst, C. E. Davoust and B. M. Hoffman, *J. Am. Chem. Soc.*, 1991, **113**, 1533–1538.
34 K. Möbius and A. Savitsky, *Appl. Magn. Reson.*, 2022, **54**, 207–287.
35 A. Ashuiev, M. Humbert, S. Norsic, J. Blahut, D. Gajan, K. Searles, D. Klose, A. Lesage, G. Pintacuda, J. Raynaud, V. Monteil, C. Copéret and G. Jeschke, *J. Am. Chem. Soc.*, 2021, **143**, 9791–9797.
36 R. de Beer, H. Barkhuijsen, E. L. de Wild and R. Merks, *Fourier Transformation of two-dimensional spin-echo ENDOR*, 1980, **https://ismar.org/wp-content/uploads/2021/09/BMR_02_1980.pdf**.
37 S. Deblon, L. Liesum, J. Harmer, H. Schönberg, A. Schweiger and H. Grützmacher, *Chem. – Eur. J.*, 2002, **8**, 601–611.
38 G. Jeschke and A. Schweiger, *Chem. Phys. Lett.*, 1995, **246**, 431–438.
39 N. Yang, M. Reiher, M. Wang, J. Harmer and E. C. Duin, *J. Am. Chem. Soc.*, 2007, **129**, 11028–11029.
40 D. Goldfarb, B. Epel, H. Zimmermann and G. Jeschke, *J. Magn. Reson.*, 2004, **168**, 75–87.
41 B. Epel and D. Goldfarb, *J. Magn. Reson.*, 2000, **146**, 196–203.
42 G. Jeschke and A. Schweiger, *J. Chem. Phys.*, 1995, **103**, 8329–8337.
43 C. Bühlmann, A. Schweiger and R. Ernst, *Chem. Phys. Lett.*, 1989, **154**, 285–291.
44 V. Y. Zevin and A. Brik, *Sov. Phys. Solid State.*, 1972, **13**, 2913.
45 T. Abramovskaya, B. Berulava and T. Sanadze, *Zh. Eksp. Teor. Fiz.*, 1974, **66**, 306–312.
46 T. Wacker and A. Schweiger, *Chem. Phys. Lett.*, 1992, **191**, 136–141.
47 T. Wacker, G. A. Sierra and A. Schweiger, *Isr. J. Chem.*, 1992, **32**, 305–322.
48 A. Doll and G. Jeschke, *J. Magn. Reson.*, 2014, **246**, 18–26.
49 D. Kunz, *Magn. Reson. Med.*, 1986, **3**, 377–384.
50 J. Bohlen and G. Bodenhausen, *J. Magn. Reson., Ser. A*, 1993, **102**, 293–301.
51 N. Wili and G. Jeschke, *J. Magn. Reson.*, 2018, **289**, 26–34.
52 J. Stropp, N. Wili, N. C. Nielsen and D. Klose, *Magn. Reson.*, 2025, **6**, 33–42.
53 S. Stoll and A. Schweiger, *J. Magn. Reson.*, 2006, **178**, 42–55.
54 F. Canonica, D. Klose, R. Ledermann, M. M. Sauer, H. K. Abicht, N. Quade, A. D. Gossert, S. Chesnov, H.-M. Fischer, G. Jeschke, H. Hennecke and R. Glockshuber, *Sci. Adv.*, 2019, **5**, eaaw8478.
55 R. Tschaggelar, B. Kasumaj, M. G. Santangelo, J. Forrer, P. Leger, H. Dube, F. Diederich, J. Harmer, R. Schuhmann, I. García-Rubio and G. Jeschke, *J. Magn. Reson.*, 2009, **200**, 81–87.
56 A. Doll, S. Pribitzer, R. Tschaggelar and G. Jeschke, *J. Magn. Reson.*, 2013, **230**, 27–39.

57 J. Stropp, D. Klose and N. Wili, *Experimental data, processing and simulation scripts for CHEESY ENDOR*, 2025, DOI: **10.5281/zenodo.17492056**.
58 N. Wili, S. Richert, B. Limburg, S. J. Clarke, H. L. Anderson, C. R. Timmel and G. Jeschke, *Phys. Chem. Chem. Phys.*, 2019, **21**, 11676–11688.
59 N. Cox, A. Nalepa, W. Lubitz and A. Savitsky, *J. Magn. Reson.*, 2017, **280**, 63–78.
60 R. Rizzato, I. Kaminker, S. Vega and M. Bennati, *Mol. Phys.*, 2013, **111**, 2809–2823.
61 A. Kehl, L. Sielaff, L. Remmel, M. L. Rämisch, M. Bennati and A. Meyer, *Phys. Chem. Chem. Phys.*, 2025, **27**, 1415–1425.
62 L. Sielaff, A. Kehl, A. Aden, A. Meyer and M. Bennati, *Sci. Adv.*, 2025, **11**, eady5665.
63 J. Stropp, MSc thesis, ETH Zurich, 2021.
64 A. Potapov, B. Epel and D. Goldfarb, *J. Chem. Phys.*, 2008, **128**, 052320.
65 J. E. Roberts, J. F. Cline, V. Lum, H. B. Gray, H. Freeman, J. Peisach, B. Reinhammar and B. M. Hoffman, *J. Am. Chem. Soc.*, 1984, **106**, 5324–5330.
66 M. Shanmugam, J. Wilcoxen, D. Habel-Rodriguez, G. E. Cutsail III, M. L. Kirk, B. M. Hoffman and R. Hille, *J. Am. Chem. Soc.*, 2013, **135**, 17775–17782.
67 J. J. L. Morton, A. M. Tyryshkin, R. M. Brown, S. Shankar, B. W. Lovett, A. Ardavan, T. Schenkel, E. E. Haller, J. W. Ager and S. A. Lyon, *Nature*, 2008, **455**, 1085–1088.
68 A. Raitsimring, K. Salikhov, B. Umanskii and Y. D. Tsvetkov, *Fiz. Tverd. Tela*, 1974, **16**, 756–766.
69 J. R. Klauder and P. W. Anderson, *Phys. Rev.*, 1962, **125**, 912–932.
70 C. E. Tait and S. Stoll, *J. Magn. Reson.*, 2017, **277**, 36–44.
71 J.-B. Verstraete, W. K. Myers and M. Foroozandeh, *J. Chem. Phys.*, 2021, **154**, 9094201.